Toward an Uncertainty Budget for a Coastal Ocean Model

SANGIL KIM AND R. M. SAMELSON

College of Oceanic and Atmospheric Sciences, Oregon State University, Corvallis, Oregon

CHRIS SNYDER

National Center for Atmospheric Research, Boulder, Colorado*

(Manuscript received 22 January 2010, in final form 31 August 2010)

ABSTRACT

Estimates of three components of an uncertainty budget for a coastal ocean model in a wind-forced regime are made based on numerical simulations. The budget components behave differently in the shelf regime, inshore of the 200-m isobath, and the slope-interior regime, between the 200-m isobath and a fixed longitude (126°W) that is roughly 150 km offshore. The first of the three budget components is an estimate of the uncertainty in the ocean state given only a known history of wind stress forcing, with errors in the wind forcing estimated from differences between operational analyses. It is found that, over the continental shelf, the response to wind forcing is sufficiently strong and deterministic that significant skill in estimating shelf circulation can be achieved with knowledge only of the wind forcing, and no ocean data, for wind fields with these estimated errors. The second involves initial condition error and its influence on uncertainty, including both error growth with time from well-known initial conditions and error decay with time from poorly known initial conditions but with well-known wind forcing. The third component is that of boundary condition error and its influence on the interior solutions, including the dependence of that influence on the specific location along the boundary of the boundary condition error. Boundary condition errors with amplitude comparable to the root-mean-square variability at the boundary lead eventually to errors equal to the root-mean-square variability in the slope-interior regime, and somewhat smaller errors in the shelf regime. Covariance estimates based on differences of the wind-forced solutions from the ensemble mean are not dramatically different from those based on the full fields, and do not show strong state dependence.

1. Introduction

As numerical forecasts of coastal ocean flows become feasible, the predictability of such flows and the processes controlling it are of increasing interest. For the wind-forced Oregon coastal ocean regime, Kim et al. (2009) recently examined the growth of initial condition differences in simulations forced by identical, spatially uniform, time-dependent winds based on buoy observations. The present study extends the results of Kim et al. (2009) to address the dependence of uncertainty in the coastal ocean state on uncertainty in the wind forcing, in the initial conditions, and in the lateral boundary conditions, and by considering regional forecast-model analysis wind-forcing fields containing the strong spatial variations known to be induced by orographic and other effects.

Predictions of the coastal ocean are influenced by a unique combination of processes. In coastal upwelling regimes such as that considered here, the mean wind stress drives Ekman transport away from the coast, resulting in upwelling of deep waters along the coast. The resulting tilting of density surfaces implies a geostrophic alongshore coastal jet; such a jet dominates the climatological ocean flow in the domain we consider. This jet interacts with the alongshore variations in coastal topography, and develops instabilities, producing a variety of nearshore eddies with preferred locations. Over the continental shelf, variations in the alongshore wind stress also force poleward-propagating, coastally trapped waves, essentially as a linear, forced, damped response to the fluctuating wind stress.

* The National Center for Atmospheric Research is sponsored by the National Science Foundation.

Corresponding author address: Sangil Kim, College of Oceanic and Atmospheric Sciences, Oregon State University, Corvallis, OR 97331.
E-mail: skim@coas.oregonstate.edu

DOI: 10.1175/2010MWR3352.1

We design our experiments around the intuitive notion of an uncertainty budget for the coastal ocean, in the following sense. Suppose that we wish to forecast the coastal ocean using a numerical model. Our forecast will be subject to error and thus be uncertain because the initial state of the ocean in the model's domain, the conditions along the domain's lateral boundary, the wind stress (and possibly other atmospheric forcing) at the ocean surface, and the ocean dynamics as embodied in the model equations are all known only imperfectly. Our goal is to quantify the contributions to uncertainty in the coastal ocean forecast from uncertainty in the initial conditions, lateral boundary conditions, and wind forcing. We will ignore the additional source of uncertainty arising from imperfections in the forecast model; this allows us to consider only differences among solutions produced by a single numerical model. Although more sophisticated approaches are possible, we will generally measure uncertainty using an appropriately normalized, volume-integrated variance.

Elements of a similar uncertainty budget have been developed over the last 20 yr for limited-area atmospheric predictions. Dynamical error growth, internal to the domain, is clearly important, both at the $O(10^3$ km) scale of midlatitude baroclinic eddies (e.g., Ehrendorfer and Errico 1995) and, if the model has sufficient resolution, at smaller scales where error growth can be energized by moist processes (Zhang et al. 2003). Lateral boundary conditions also play a key role, especially as the domain size decreases (Vukićević and Errico 1990). Uncertainty at the lower boundary, either in the land surface state or the sea surface temperature, can have noticeable effects as well (Sutton et al. 2006), though their importance appears to be less than that of uncertainty in wind stress on the coastal ocean simulations examined here.

The outline of the paper is as follows. The basic model configuration is described in section 2. Numerical experiments addressing uncertainty in wind forcing, initial conditions, and boundary conditions are presented in sections 3, 4, and 5, respectively. Error covariance structures estimated from the wind-forcing ensemble are presented in section 6. The main results are summarized in section 7.

2. Numerical model: The Oregon Coastal Transition Zone

a. Model configuration

For these simulations, we adopt the nested grid model configuration for the Oregon Coastal Transition Zone (OCTZ) implemented by Springer et al. (2009), who studied the upwelling circulation in the OCTZ region during summer 2001, and showed that this model reproduces relatively realistic OCTZ circulation features including shelf flow over the Heceta Bank, coastal jet separation and eddy formation offshore of Cape Blanco, and jet and eddy evolution in the offshore region. Simulations with this model configuration represent the OCTZ more faithfully than the periodic-channel domain used in related studies by Oke et al. (2002a,b,c), Kurapov et al. (2005a,b), and Kim et al. (2009).

The Springer et al. (2009) OCTZ implementation uses a three-dimensional free-surface and hydrostatic primitive equation model discretized over abruptly varying topography with terrain-following σ coordinates. The numerical code used is based on the Regional Ocean Modeling System (ROMS) described by Shchepetkin and McWilliams (2005). The model domain ranges from 40° to 47.5°N and from 123.7° to 129°W, and the grid resolution is about 3.1 km, with 136 and 250 grid points of latitude and longitude, respectively (Fig. 1). The configuration has 40 σ layers in the vertical, with enhanced resolution near the surface and bottom corresponding to stretching parameters $q_b = 0.2$ and $q_s = 6.0$ (Song and Haidvogel 1994). The realistic bathymetry is obtained by bilinearly interpolating the 5-min gridded elevations/bathymetry for the world (ETOPO-5; National Geophysical Data Center 1988) and then smoothing with an r factor of 0.2 to limit the pressure gradient error associated with the terrain-following coordinate (Beckmann and Haidvogel 1993), and the Coriolis force varies with latitude. Vertical mixing is computed using the "level 2.5" scheme of Mellor and Yamada (1982), while the horizontal diffusivity and viscosity are 20 $m^2\ s^{-1}$.

The model domain has a closed, coastal eastern boundary with no normal flow and free-slip conditions, and open boundaries on the north, south, and west (Fig. 1). Chapman (1985) and Flather (1976) conditions are prescribed for the free-surface elevation and depth-averaged velocities, respectively, normal to the open boundaries. The open-boundary data are provided every 12 h by the model output of 2001 in the Navy Coastal Ocean Model (NCOM) and the California Current System (CCS; Shulman et al. 2004). Following the best nesting strategy found by Springer et al. (2009), radiation and nudging conditions are applied at all open boundaries for both the three-dimensional velocities and tracers of temperature and salinity, and sponge layers are adopted at the western and southern boundaries, using diffusivity and viscosity equal to 100 $m^2\ s^{-1}$ and tapered over 150 km to their interior values. The model includes neither freshwater nor salinity flux through the ocean's surface and no tidal forcing, and the heat fluxes are calculated from the bulk flux formulation of Fairall et al. (1996).

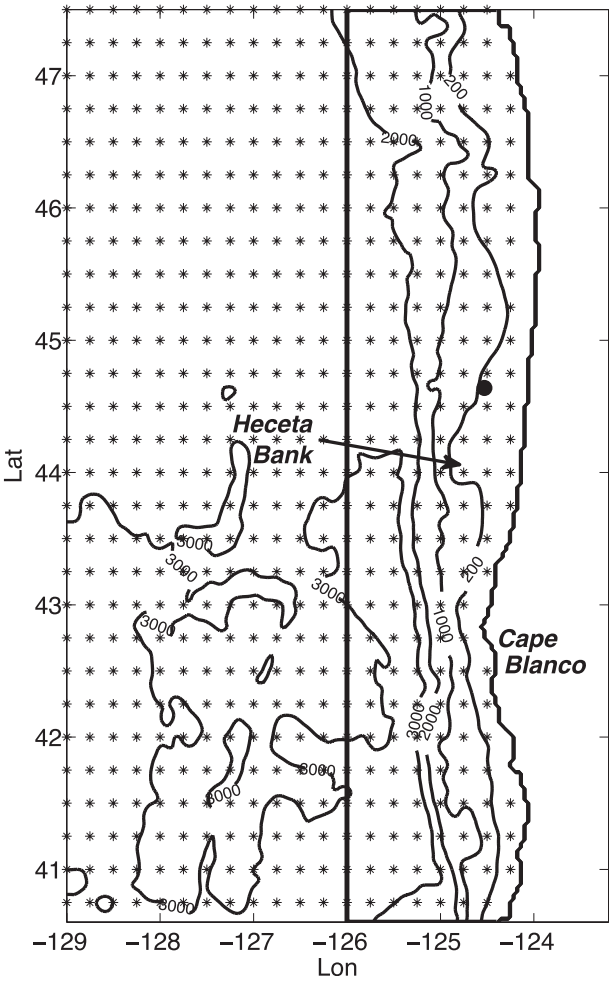

FIG. 1. Model domain with smoothed bottom topography (0, 200, 1000, 2000, and 3000 m). The region between 126°W and the coastline is the subdomain where statistical quantities are calculated. The asterisks are the locations of extracted wind data from TIGGE. The thick dot indicates the location of NDBC buoy 46050 at 44.64°N, 124.53°W.

b. Shelf and slope-interior regions

To obtain results separately in the dynamically distinct shelf and slope-interior regimes, we divide the model domain into two subdomains, a shelf region from the coastline to the 200-m isobath and a slope-interior region from the 200-m isobath offshore to 126°W.

For both onshore and offshore regions, we will measure the dispersion of the ensemble using a scaled ensemble variance defined by

$$N^2(t) = \frac{1}{2}\left[\frac{\langle\overline{\Delta\rho^2}\rangle}{\sigma_\rho^2} + \frac{\langle\overline{|\Delta\mathbf{u}|^2}\rangle}{\sigma_u^2 + \sigma_v^2}\right]. \tag{2.1}$$

Here, $\Delta\rho(\mathbf{x}, t) = \rho(\mathbf{x}, t) - \overline{\rho}(\mathbf{x}, t)$ and $\Delta\mathbf{u}(\mathbf{x}, t) = \mathbf{u}(\mathbf{x}, t) - \overline{\mathbf{u}}(\mathbf{x}, t)$; overbars denote ensemble averages while $\langle\cdot\rangle$ is a volume average over a specified subdomain; and σ_ρ^2 is the temporal variance of the density ρ in the simulations averaged over the ensemble and over the subdomain, with σ_u^2 and σ_v^2 defined similarly for the two components u and v of the horizontal velocity vector $\mathbf{u}$. We will refer to N, the square root of this scaled variance, as the ensemble spread; note that $N = 1$ when the volume- and ensemble-averaged squared differences for density and horizontal velocity are equal to the respective squared standard deviations σ_ρ^2 and $\sigma_u^2 + \sigma_v^2$.

c. Basic case

For the basic-case simulation, the model configuration and surface forcing is the same as that used by Springer et al. (2009). The ocean initial and boundary conditions were obtained from spatial interpolation of the NCOM–CCS output, with the initial conditions taken from day 120 and the boundary information linearly interpolated in time between twice-daily NCOM–CCS output files. The ocean is forced by spatially variable wind stress from the Coupled Ocean–Atmosphere Mesoscale Prediction System (COAMPS) reanalysis for the year 2001 (Kindle et al. 2002).

Averaged over the shelf subdomain, the COAMPS winds are southward and upwelling favorable at greater than 1 m s^{-1} during 78% of the simulation period and northward and downwelling favorable at greater than 1 m s^{-1} during only 14% of the simulation period (Fig. 2c). Averaged over the simulation period, the spatially averaged shelf meridional and zonal winds are −4.1 and 1.4 m s^{-1}, respectively. This wind stress implies, on average, Ekman transport away from the coast and therefore to coastal upwelling, which in turns leads to the development of sloping isopycnals adjacent to the coast and an associated alongshore geostrophic jet. The temporal mean of this surface current has a maximum speed exceeding 0.45 m s^{-1} (Fig. 2c). The COAMPS wind analysis during this period also captures well the orographically intensified jet (Samelson et al. 2002; Perlin et al. 2004) southwest of Cape Blanco (Fig. 2a). Consistent with this intensification of the winds from north to south, there is a southward intensification of the wind-driven geostrophic upwelling jet. There is additional mesoscale variability of the surface current associated with seafloor topographic features, especially Heceta Bank and the slope and shelf topography near Cape Blanco (Figs. 1 and 2). Around the southern side of the Heceta Bank, where the shelf narrows abruptly, the mean southward jet crosses isobaths and trends offshore. Around the southern Oregon shelf near Cape Blanco, there is persistent offshore flow with separation of the mean coastal jet from the 200-m isobath near the tip of Cape Blanco (42°N).

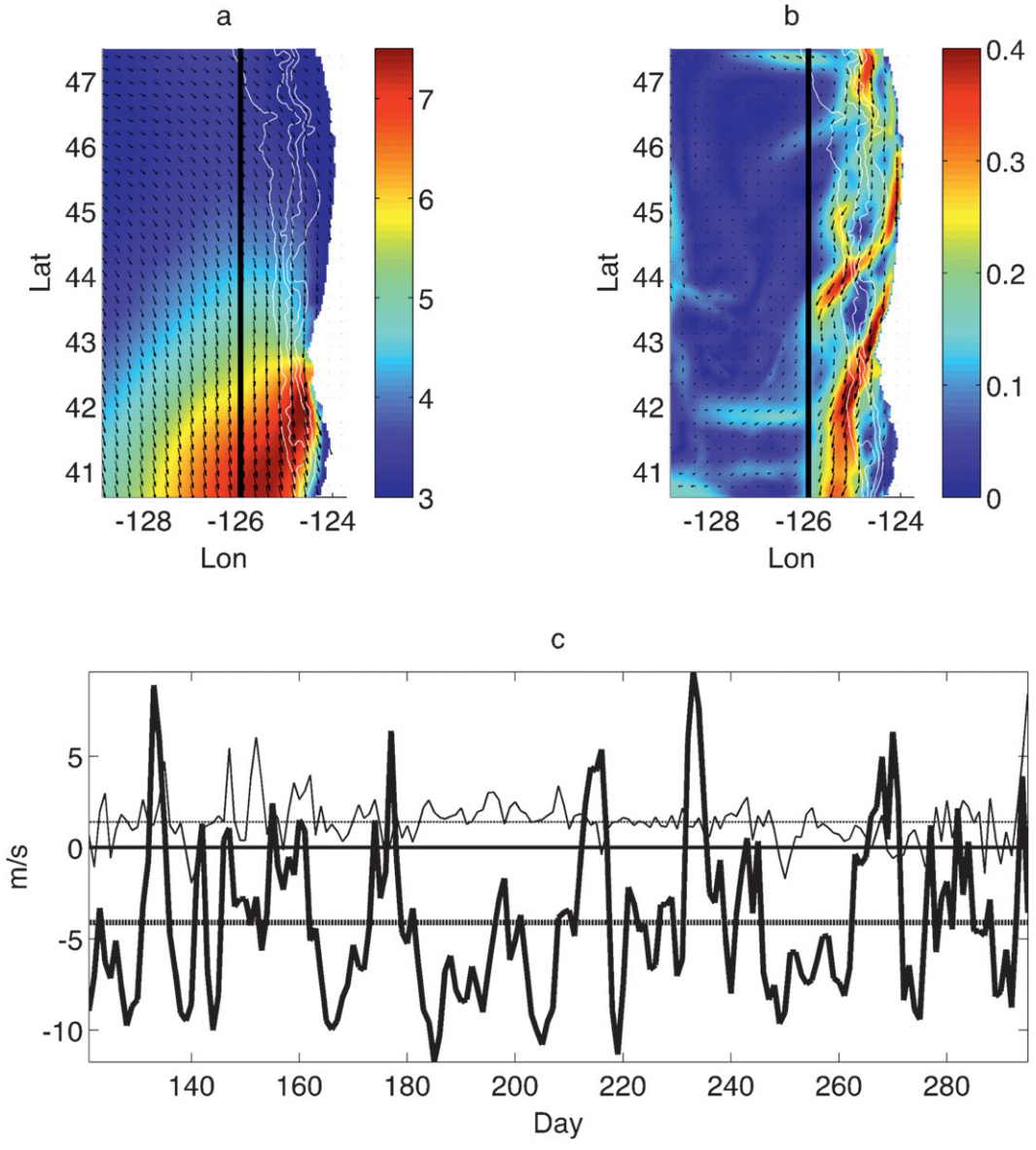

FIG. 2. Temporal mean of COAMPS (a) wind of 2001 and (b) sea surface current for days from 120 to 295. Color represents the speed (m s^{-1}) for wind and ocean surface current with velocity vector plotted at every seventh grid point. The vertical black lines represent 126°W. Topographic contours (200, 1000, 2000, and 3000 m) are indicated by white lines. (c) Area-averaged meridional (thick solid) and zonal wind (thin solid) at 10 m from ocean surface over the subdomain. No wind (0 m s^{-1}) is indicated by the thick straight line, and the means of the area averaged for meridional (−4.1 m s^{-1}) and zonal (1.4 m s^{-1}) winds are indicated by the thick and thin dotted lines, respectively.

The general characteristics of the coastal ocean response to the mean upwelling-favorable wind during the simulation period are broadly consistent both with observations (Castelao and Barth 2005; Barth et al. 2000; Kosro 2005) and with previous numerical model results for this region obtained with similar model configurations (Kurapov et al. 2005a,b; Springer et al. 2009). There is evidence of artificial boundary effects adjacent to the northern boundary, but these effects are primarily limited to the latter part of the simulation. Thus, the simulations can be anticipated to have sufficient skill that a more detailed examination of their uncertainty properties is warranted.

3. Uncertainty in wind stress

This section presents results from experiments in which the wind forcing is uncertain, but the initial and lateral

boundary conditions are assumed known. We first describe the ensemble of wind forcings, which is meant to represent the uncertainty in present-day atmospheric surface analyses. Then, we analyze the results of ensembles of ocean simulations forced by the wind-analysis ensemble.

a. Wind-analysis ensemble

In the absence of ocean observations, an estimate of the ocean state may be constructed by forcing the ocean model from a random initial state with a long-term record of past winds. If the winds are sufficiently accurate, and the ocean responds strongly and deterministically to the wind forcing in the region of interest, this procedure may result in an estimate of the ocean state with useful skill. Alternatively, errors in the wind forcing will result in errors in the estimate of ocean state, as will dynamical processes that are internal to the ocean and not controlled by the wind forcing. To quantify the amplitude of the uncertainty in the ocean state that arises from uncertainty in the estimated wind forcing, an ensemble of ocean model simulations was constructed by forcing the ocean model with an ensemble of different wind fields.

The wind ensemble was constructed so that its statistics were at least broadly representative of the error in analyzed surface winds from operational numerical weather prediction centers. The ensemble mean was taken to be the COAMPS wind analysis. To obtain realistic variability of wind about this ensemble mean, we utilized the analysis wind products of year 2008 from Centro de Previsao de Tempo e Estudos Climáticos (CPTEC; Brazil), the European Centre for Medium-Range Weather Forecasts (ECMWF; Europe), the National Centers for Environmental Prediction (NCEP; United States), the Met Office (UKMO; United Kingdom), the China Meteorological Administration (CMA; China), the Japan Meteorological Agency (JMA; Japan), and the Korean Meteorological Agency (KMA; Korea), available at The Observing System Research and Predictability Experiment (THORPEX) Interactive Grand Global Ensemble (TIGGE) data archive. The wind products were bilinearly interpolated from the $0.25° \times 0.25°$ analysis product grid to the model grid points; for model grid points within 0.25° of the coastline, the analysis data from the nearest points were extrapolated toward the coast. At each analysis time, we then constructed an ensemble of winds by removing from each center's analysis the mean over the seven separate analyses and adding that deviation to the COAMPS analysis. The year 2001 COAMPS winds were used to allow cross checking of the numerical results with those of Springer et al. (2009); the use of analysis winds from the same year would perhaps have been more consistent, but these were not available for 2001. A relatively weak state dependence of the analysis differences can be expected for the synoptic conditions prevalent in the summer season, so that any biases in the estimate of analysis errors should be relatively unimportant.

Our basic assumption in constructing this wind-forcing ensemble is that the differences among the analyses are statistically similar to the errors in the analyses. To check whether the ensemble has realistic variance, we calculated the differences between each of the 7 different analysis products and the measured winds at National Data Buoy Center (NDBC) buoy 46050, located at 44.64°N, 124.53°W (Fig. 1). The RMS errors for the meridional wind vary between 0.61 and 2.18 m s^{-1} with a temporal and ensemble average of 1.20 m s^{-1}, while those for zonal wind vary between 0.56 and 2.18 m s^{-1} with an average of 1.06 m s^{-1}. These RMS errors may be compared with the time-averaged ensemble standard deviations of 1.1 and 0.45 m s^{-1} for the meridional and zonal components, respectively. The spread of the analyzed winds is therefore comparable to the errors in the winds; the agreement is worst for the zonal component, but the zonal component is generally of less importance than the meridional for the coastal ocean response. The standard deviation errors of the analysis winds are also substantially smaller than the corresponding measured values of 5.8 and 1.6 m s^{-1} for the meridional and zonal components, respectively, indicating that the analysis winds generally estimate the buoy winds with substantial skill. Previous studies have shown that this is true also for the COAMPS wind analyses.

For the summer upwelling season, the time-averaged variance of the wind speed field has a spatial structure that is similar to the temporal mean (Fig. 2a; see also, e.g., Perlin et al. 2004). The spatial structure of the time-averaged ensemble standard deviation of wind speed differences is broadly similar to both of these, with intensification near the coast and to the south of Cape Blanco, where maximum values of the ensemble standard deviation reach 2.5 m s^{-1} (Fig. 3a). The spatially averaged standard deviation of the winds over the shelf subdomain has a time mean of 1.1 and 0.8 m s^{-1} for the meridional and zonal winds, respectively, with substantial variability in time (Fig. 3c). Examination of time-averaged wavenumber power spectra shows that the ratio of the ensemble wind-difference variance to the COAMPS mean-wind variance is nearly independent of spatial scale (Fig. 4). Thus, this method gives wind perturbations that have the same spatial dependence in amplitude as do the unperturbed wind fields themselves, rather than focusing on the perturbations at a particular spatial scale. For the wind-difference fields, correlations of 0.5 and larger are found for the alongshore component on alongshore scales comparable to the domain size, while correlation

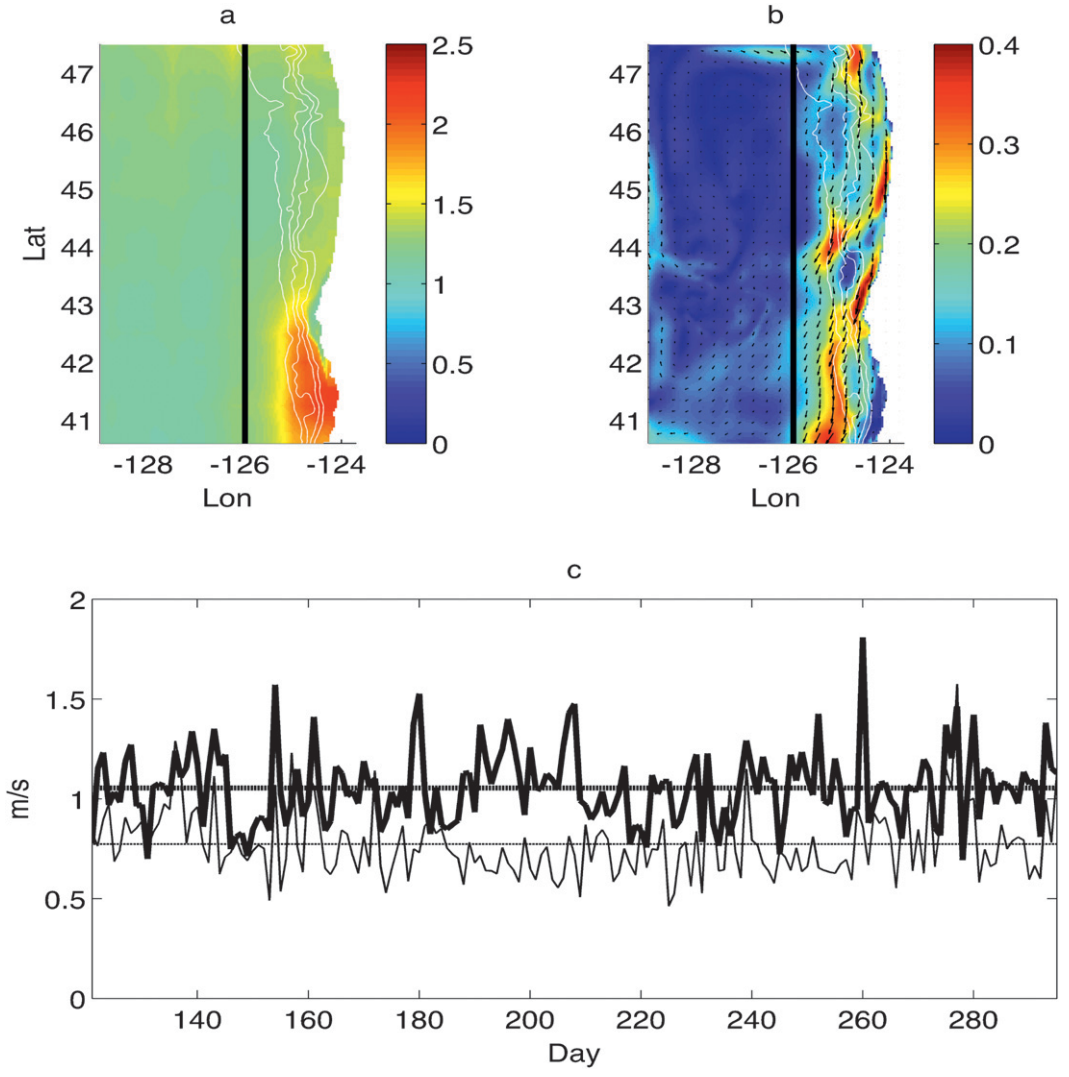

FIG. 3. (a) Temporal mean of the time series of the standard deviations of the ensemble of analysis winds from the corresponding instantaneous ensemble means for days 120–295. (b) Ensemble and temporal means of sea surface current for days 120–295. Color represents the speed (m s^{-1}) for surface current with velocity vector plotted at every seventh grid point. Topographic contours (200, 1000, 2000, and 3000 m) are shown with white lines. (c) Area- and ensemble-averaged RMS error for meridional (thick solid) and zonal (thin solid) wind relative to the ensemble mean over subdomain. Temporal average for meridional (thick dotted, 1.1 m s^{-1}) and zonal (thin dotted, 0.8 m s^{-1}).

scales for the zonal component, and cross-shore correlation scales for both components, are significantly shorter (Fig. 4).

The approach taken here is one of many that could have been used to estimate wind analysis errors (e.g., Mourre et al. 2004; Barth et al. 2008; Vandenbulcke et al. 2008; Bèal et al. 2010; Broquet et al. 2008; Leeuwenburgh 2005; Lucas et al. 2008; Jordà and De Mey 2010; Burillo et al. 2002). The perturbation of wind fields are generally obtained either by the empirical orthogonal functions (EOFs) computed from difference fields between different sources of winds or Monte Carlo method taking wind fields from different years. Since the actual uncertainty of wind fields in this study could be represented by a total variability of winds at the same year, the approach of the Monte Carlo method is employed rather than using the EOFs. The comparisons above suggest that the approach provides a useful estimate of the amplitude and scale of the dominant errors that are relevant for the coastal ocean response.

b. *Ocean ensemble*

From the wind-analysis ensemble described above, an ensemble of ocean simulations was constructed by forcing

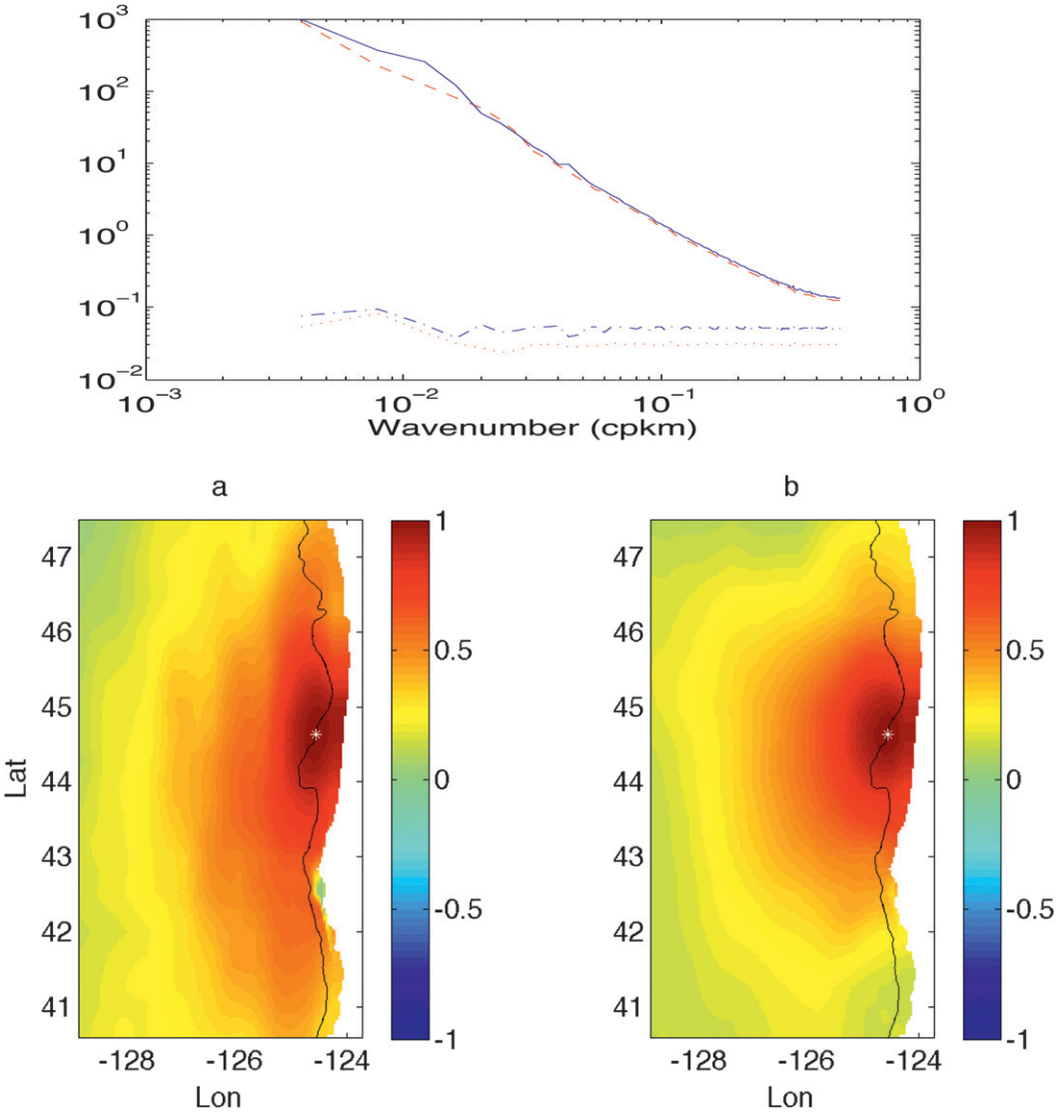

FIG. 4. (top) Time mean of wavenumber power spectra ($m^2\ s^{-2}$ $cpkm^{-1}$; cpkm is cycles per kilometer) for COAMPS along 125° (solid) and 126°W (dashed), and ratio of time-mean ensemble-difference wavenumber power spectra to time mean of COAMPS wavenumber power spectra along 125° (dash–dotted) and 126°W (dotted). (bottom) (a) Ensemble-averaged temporal correlations of the differences of the wind-forcing ensemble meridional wind at each point with the corresponding differences at the intersection (asterisk) of the NH line and the 200-m isobath; (b) as in (a), but for zonal wind.

the model with each of the seven members of the wind-analysis ensemble. Each member of the ensemble of simulations used the same ocean initial and boundary conditions as the basic case. Like the basic case, the resulting ensemble members were all integrated from day 120 to day 295 of 2001.

The time- and ensemble-mean ocean surface velocity vectors from this ensemble show basic similarities to the time mean of the basic case (Fig. 3b). The large surface currents over the shelf and slope represent the geostrophic response to the generally upwelling-favorable winds, including the orographic intensification associated with Cape Blanco. Offshore extensions of the alongshore upwelling jet are found south of Heceta Bank and Cape Blanco, though these differ between the ensemble mean and the basic case more than do the mean surface currents over the shelf. Relative to the time- and ensemble-mean surface current, the ensemble-mean standard deviation of surface current is generally larger over the slope-interior regime than over the shelf (Figs. 5a and 3b). Cross sections of the standard deviation of horizontal velocity at 42.17°N, 125°W and have maxima near Cape Blanco, and

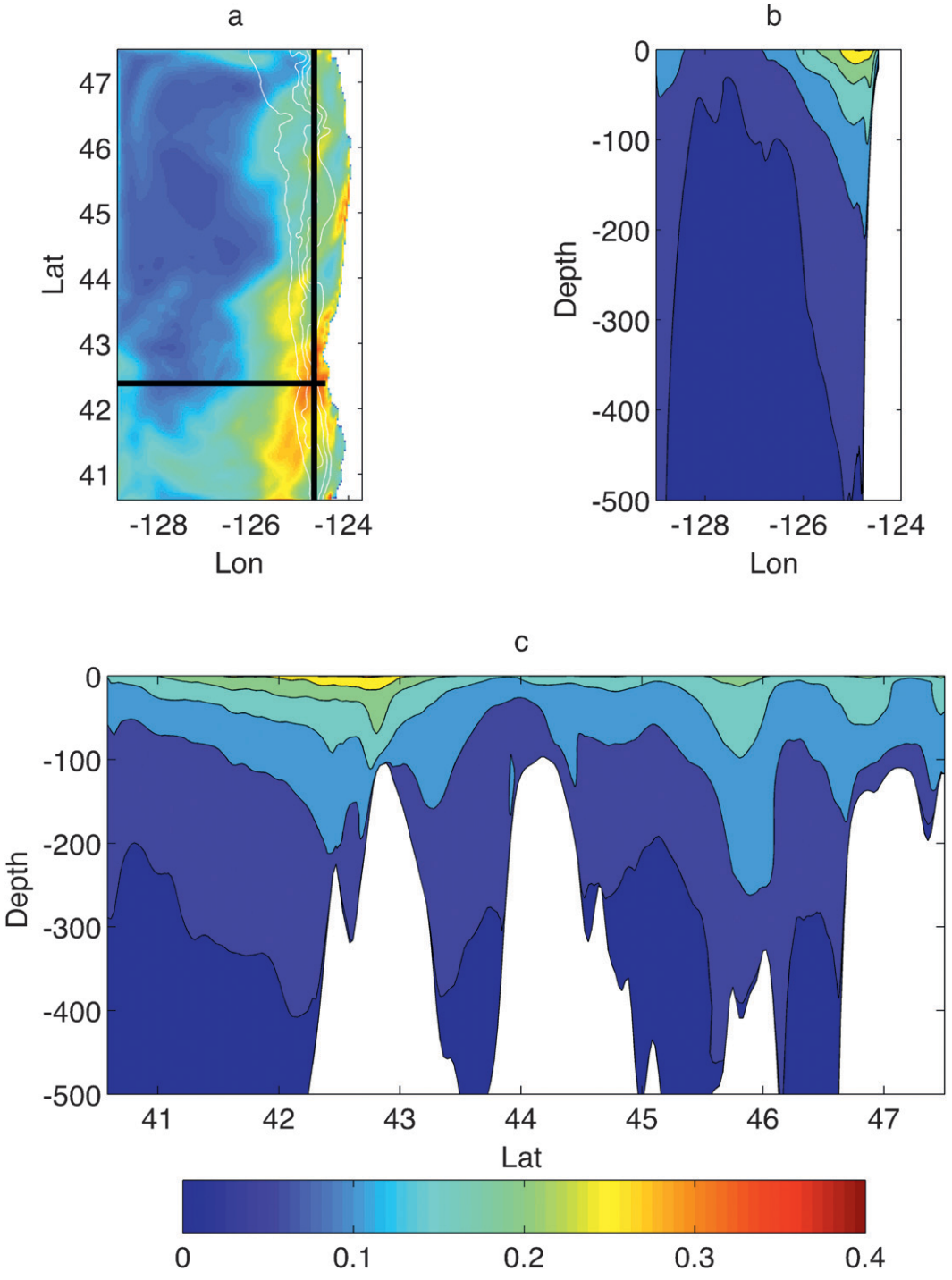

FIG. 5. Ensemble and temporal standard deviation of horizontal velocity for days 120–295 for (a) surface, (b) across-shore vertical section at 42.17°N, and (c) alongshore vertical section at 125°W. Topographic contours (200, 1000, 2000, and 3000 m) are indicated by white lines; the black horizontal and vertical lines are at 42.37°N and 125°W, respectively.

show that most of the variability is restricted to depths less than 50 m (Figs. 5b,c).

The qualitative differences in the shelf and slope-interior ensemble dynamics can be quantified by computing the normalized standard deviation N, defined in (2.1), as a function of time for each subdomain. For both onshore and offshore regions, this ensemble spread N grows over the first 10 days of the simulation period (Fig. 6). In the

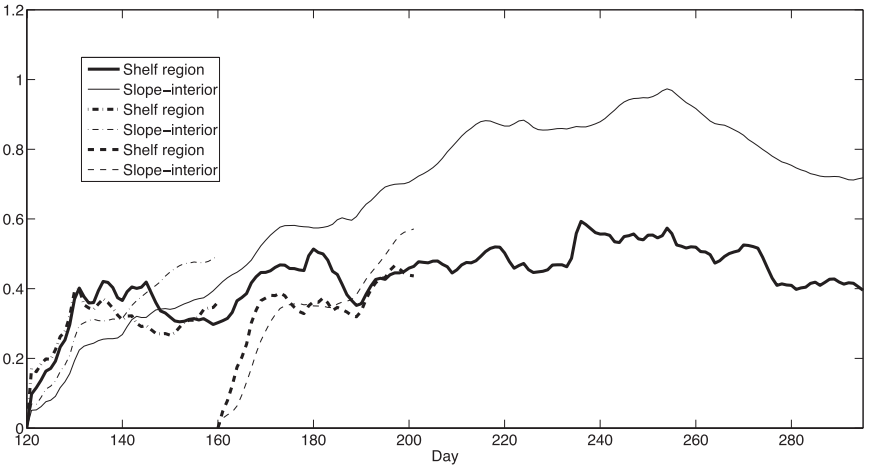

FIG. 6. Ensemble spread as a function of time for experiments using the ensemble of wind forcings described in section 3a and no uncertainty in the initial or lateral boundary conditions. Thick and thin lines represent the shelf region (between the coast and the 200-m isobath) and the slope region (between the 200-m isobath and 126°W), respectively. Solid lines indicate experiments using the same initial conditions as the basic case. Dash–dotted and dashed lines are for experiments that begin at days 120 and 160, respectively, and whose initial conditions are taken from the day-160 fields of a single ensemble member from the first experiment.

offshore region, N then grows steadily but more slowly over the next 100 days to a value near unity, and remains near that value for the rest of the period. In the onshore region, N does not grow consistently after the first 10 days; instead, it fluctuates around a value of 0.4 for the rest of the period (Fig. 6).

The limited growth of the normalized ensemble spread over the coastal regions indicates that the deterministic coastal ocean response to the ensemble-mean wind forcing dominates the uncertainty arising both directly from the variations of the forcing about the mean and indirectly through the differing development of instabilities and other internal dynamical processes. This contrasts with the behavior offshore, which is presumably dominated by the development of instabilities, as the deterministic response to the ensemble-mean wind forcing plays a much smaller role in the deep ocean. The time scale for the initial error growth is then set by the spinup time scale over which differences in wind forcing lead to differences in the upwelling jet and by the time scale of the shallow instabilities of the upwelling jet, while the longer time scale in the rest of the domain is associated with offshore baroclinic disturbances, which generally have a larger vertical scale and a longer time scale.

This experiment on initial error growth with uncertainty in the wind forcing was repeated twice to test the sensitivity of the result to the initial state and to the character of the ensemble-mean wind forcing. For both of these additional experiments, the initial ocean state was taken from one member of the original ensemble at day 160. Then, two ensembles of simulations with this initial state were integrated for 40 days, with forcing starting at days 120 and 160, respectively, of the wind-analysis ensemble. Consistent with the original results, these simulations show that the growth of the ensemble spread for the offshore region is initially less than that for the onshore region and that this later reverses so that, as before, the normalized ensemble spread for the onshore region reaches a quasi-equilibrium near 0.4, while that for the offshore region appears to continue to grow toward larger values (Fig. 6, dashed and dash–dotted lines).

4. Uncertainty in initial conditions

Initial condition error and its influence on uncertainty appear in at least two different contexts. With exact or well-known initial conditions, initial errors will grow with time because of internal dynamical processes and errors in forcing and boundary conditions, as was seen in the previous section. With poorly known initial conditions and relatively well-known forcing and boundary conditions, initial errors may decay with time if the deterministic response to forcing is sufficiently strong.

In this section, we consider the error growth characteristics for sets of simulations with differing initial conditions but identical forcing. For this analysis, the initial conditions were taken as the seven states of the original analysis-wind ensemble simulations on each of the 7 days: 140, 160, 180, 200, 220, 240, and 260, for 49 total initial

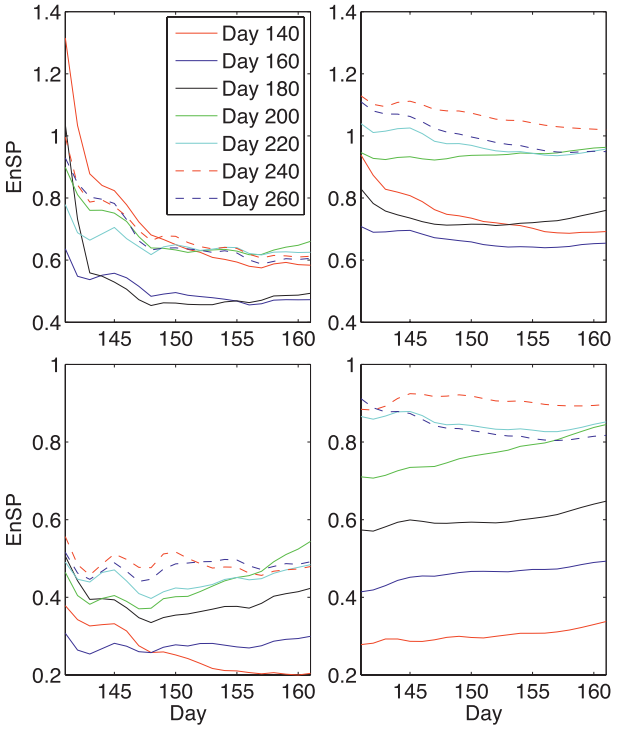

FIG. 7. Ensemble spread N vs day for seven sets of seven simulations with initial conditions taken from the indicated days and wind-forcing from COAMPS for days 140–160. (top) N computed with respect to the ensemble mean of all 49 simulations. (bottom) N computed with respect to the ensemble mean for each seven-member ensemble with initial conditions from a given day. (left) N computed in the region between the coastline and the 200-m isobath. (right) N computed in the region between the 200-m isobath and 126°W.

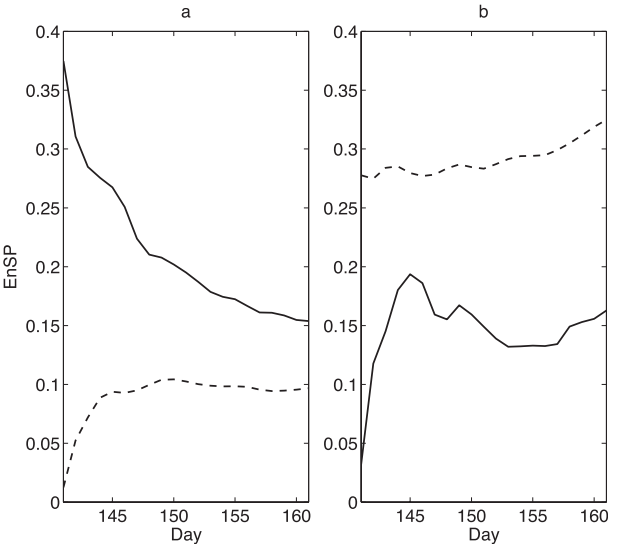

FIG. 8. N vs day for seven simulations with initial conditions taken from day 140 and wind forcing from COAMPS for days 140–160. The initial conditions were set to the ensemble mean (a) offshore of the 200-m isobath and (b) onshore of the 200-m isobath. In both (a) and (b), N computed for the difference fields from the ensemble mean of the seven simulations is shown vs time for the region between the coastline and the 200-m isobath (solid line) and the region between the 200-m isobath and 126°W (dashed line).

conditions. These 49 initial conditions were then integrated for 20 days, with identical forcing from days 140–160 of the COAMPS wind field.

Relative to the ensemble mean of all 49 simulations, N in the coastal regime shows systematic decay toward the quasi-equilibrium value near 0.5 (Fig. 7). In the offshore regime, there is no such systematic decay, and N is near unity. This is consistent with the interpretation given above of the quasi-equilibrium response of the wind-analysis ensemble: in the coastal regime, the deterministic response to the wind forcing controls roughly 60% of the variance, while in the offshore regime, the variance is controlled by internal dynamics, and little deterministic response to the wind forcing can be distinguished. The time scale for the spread's evolution is also clearly faster near the coast than offshore, again consistent with results in the previous section for ensembles of wind forcing.

The ensembles of states for each of the seven initial times may also be considered separately. For example, the seven simulations with initial conditions from day 140 can be considered as an ensemble and the evolution of the spread about their mean (Fig. 7, bottom panels). In the coastal regime, the behavior of this spread varies substantially across the different ensembles, decaying initially for some of the ensembles, growing weakly at later times for some, and having little trend for others. Offshore, the spread grows slowly but steadily for all the ensembles with initial spread below 0.8. The time scale for this growth is roughly 100 days, the same as for the experiment with uncertainty in wind, which indicates that the internal dynamics of the slower, baroclinic motions is responsible for the growth in both cases.

To this point, we have emphasized the apparently different dynamics of the coastal and offshore regions. A natural question is the extent to which the evolution of the spread in the two regions is coupled. The ensemble from day 140 hints that that the spread in the coastal region may be maintained partly by interaction with the offshore flow, since that ensemble not only has the smallest spread offshore, but is also the only ensemble for which the spread relative to the ensemble mean decays steadily in the shelf region (Fig. 7).

To test this possibility, two additional variants of this set of simulations for the ensemble of seven simulations with initial conditions from day 140 were computed. In the first of these, all ensemble members were initialized

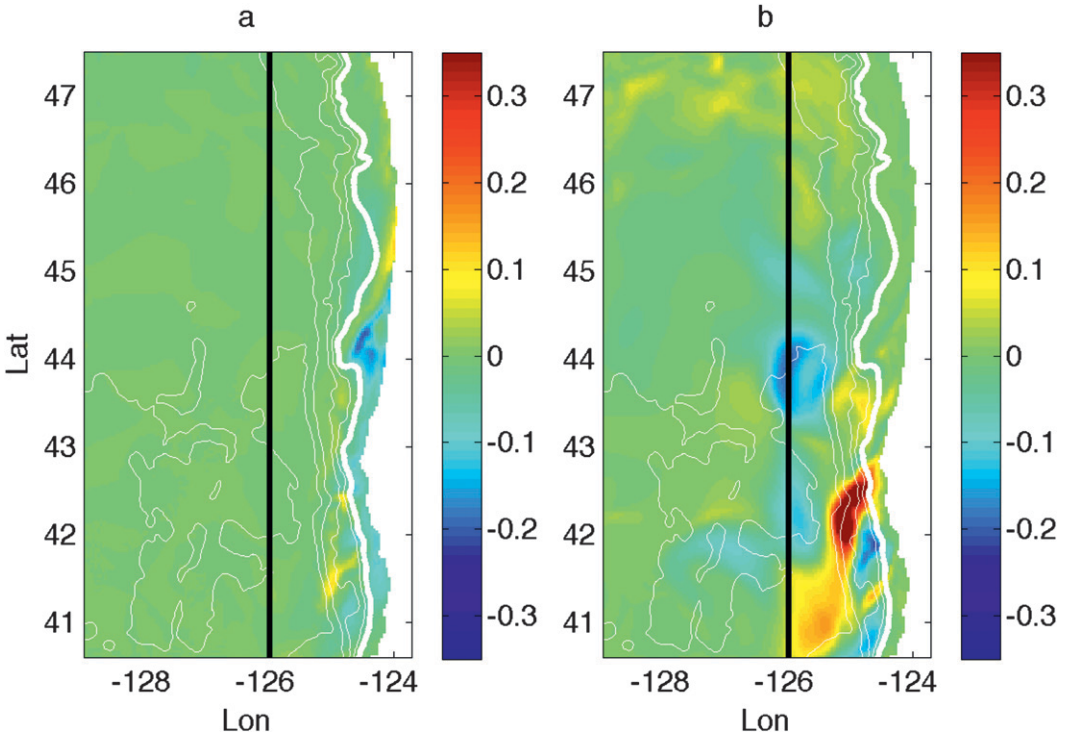

FIG. 9. Time-mean ensemble standard deviation of depth-averaged density (kg m^{-3}) for the simulations in Fig. 8 with initial conditions set to the ensemble mean (a) offshore and (b) onshore of the 200-m isobath, vs longitude and latitude. The 200-m isobath (thick white) and the 126°W meridian (black) are shown, and the color scale is the same for both (a) and (b).

with the ensemble mean fields offshore of the 200-m isobath, but with their original fields inshore of the 200-m isobath. The ensemble was then integrated for 20 days, with identical forcing from days 140 through 160 of the COAMPS wind field. The resulting decay of ensemble variance in the onshore region was more rapid than the previous case, which differed only in that the initial conditions in the offshore region were not uniform among the ensemble members (Fig. 8a). This indicates that the offshore region has a detectable dynamical influence on the onshore region, in that the offshore variance must contribute to the maintenance of the onshore ensemble variance.

In the second variant, all ensemble members were initialized with the ensemble mean fields onshore of the 200-m isobath, but with their original fields offshore of the 200-m isobath. The ensemble was again integrated for 20 days, with identical forcing from days 140 through 160 of the COAMPS wind field. In this case, as shown in (Fig. 8b), the evolution of the normalized offshore variance is almost unchanged (cf. bottom-right panel of Fig. 7), with slow, steady growth, while the normalized onshore variance grows rapidly to roughly 0.15, approximately the same value that it had decayed to in the first variant (Fig. 8a). This is consistent with the existence of dynamical influence of the offshore region on the onshore region that was inferred from the first variant.

The time-mean ensemble standard deviation of depth-averaged density for these two variants shows that the offshore variance is concentrated primarily near and south of Cape Blanco (Fig. 9). The shelf variance is instead largest near Heceta Bank in the first variant, but is contiguous with the largest offshore variance in the second variant, again suggesting an influence of the offshore region on the onshore region. The dynamics of this influence remain to be explored.

5. Boundary condition error

A third important source of error for regional coastal ocean models, in addition to surface wind stress forcing and initial condition errors, is the potential inaccuracy of conditions specified along the open boundaries. To address this source of error, including the dependence of the influence of boundary condition error on the specific location along the boundary at which it occurs, a set of simulations were carried out with prescribed differences in boundary conditions. Each of these

simulations used the same ocean initial conditions. In each case, the solutions were initialized with identical states at day 180 from the basic case, and forced with the identical COAMPS wind forcing from days 180 through 290.

a. Boundary perturbations

The prescribed boundary condition perturbations were developed as follows. First, EOFs were computed from the boundary data for all prognostic variables from days 120 to 295. Each variable was normalized by its boundary-averaged standard deviation before the EOF calculation. The resulting first three leading EOFs $\mathbf{w}_n$, where $n = 1$, 2, 3, accounted for 33%, 20%, and 13%, respectively, of the total normalized variance of the boundary data. The perturbed boundary value functions $\mathbf{B}_j(\mathbf{x}, t)$ were then obtained from these EOFs by a Karhunen–Loève expansion (Loève 1978):

$$\mathbf{B}_j(\mathbf{x},t) = \mathbf{B}_0(\mathbf{x},t) + \sum_{n=1}^{3} A_n(t) D_j(\mathbf{x}) \psi_n \sqrt{\gamma_n}\, \mathbf{w}_n(\mathbf{x}), \quad j = 1, \ldots, 4. \tag{5.1}$$

Here, $\mathbf{B}_j(\mathbf{x}, t)$ is the vector of boundary condition values for the prognostic variables at spatial location $\mathbf{x} = (x, y, z)$ and time t, $\mathbf{B}_0(\mathbf{x}, t)$ is the corresponding unperturbed boundary value function, and γ_n is the eigenvalue for boundary EOF $\mathbf{w}_n$. The mode amplitudes ψ_n are random constants independent of j, and the function $A_n(t)$ defines the temporal variability of the perturbed boundary values. The functions D_j, $j = 1, \ldots, 4$, defined below, are spatial masks, which give rise to the four independent perturbations $\mathbf{B}_j$ for each set of ψ_n. In (5.1), an additional index that would give the realization number for the set of ψ_n has been suppressed. For the first realization, the random selections resulted in $\psi_1^2 + \psi_2^2 + \psi_3^2 = 1.2$, and this sum was then forced to equal the same value for the subsequent realizations. Three realizations of ψ_n were obtained, with four perturbations $\mathbf{B}_j$, $j = \{1, \ldots, 4\}$ for each of these realizations, for a total of 12 independent boundary-perturbation simulations.

The four spatial masks $D_j, j = 1, 2, 3, 4$, were defined as follows: 1) $D_1 = 1$ everywhere, so that all boundaries were perturbed; 2) $D_2 = 2$ away from the coastal boundaries, but linearly decreasing from 1 at 126°W to 0 at 125°W along the northern and southern boundaries; 3) along the southern boundary, $D_3 = 1$ from the coastline to 125°W and linearly decreasing to 0 at 126°W, with $D_3 = 0$ everywhere else; 4) along the northern boundary, $D_4 = 1$ from the coastline to 125°W and linearly decreasing to 0 at 126°W, with $D_4 = 0$ everywhere else. The corresponding boundary perturbations $\mathbf{B}_j$, $j = \{1, \ldots, 4\}$ are referred to as the full, western, southern, and northern perturbations, respectively. For simplicity, and to limit the continuous generation of transients from the boundary perturbations, $A_n(t)$ in (5.1) was specified as time series of expansion coefficients $a_n(t)$ for the nth EOF such that $A_n(t) = a_n(t - 60)$ (shifting the mode amplitude for 60 days), and then normalized by its maximum amplitude. The corresponding shift is a typical time scale of the flow features propagation through the model boundary conditions.

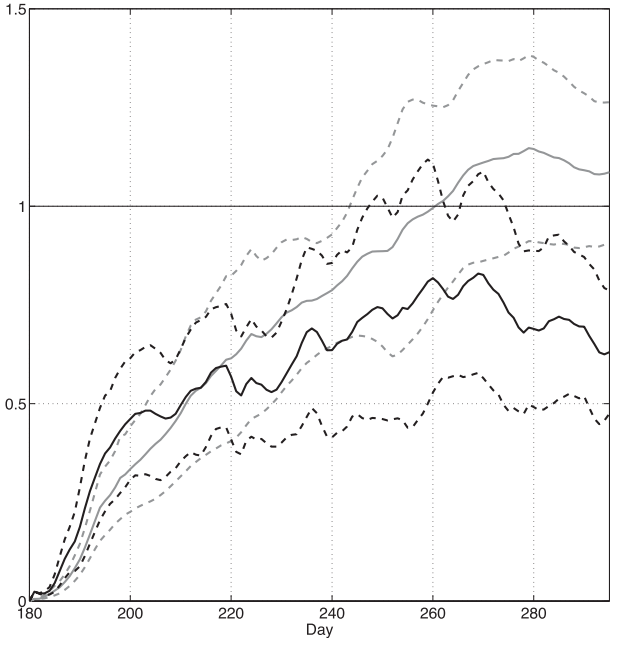

FIG. 10. Normalized ensemble variance N for the onshore (black) and offshore (gray) regions. vs time (days) for perturbed boundary condition simulations. The mean (solid) and mean ± standard deviation (dashed) of the normalized variance over three sets of four simulations, consisting of all four $\mathbf{B}_j$, $j = 1, \ldots, 4$ for each of the three independent realizations of ψ_n, are shown.

b. Ocean response

The long-term, quasi-equilibrium response to the boundary perturbations is qualitatively similar to that for the wind-analysis ensemble (Fig. 10). In the offshore region, the normalized ensemble-averaged variance N of the difference of each perturbed boundary solution from the unperturbed solution grows to unity after roughly 70–80 days, at which point the differences between solutions are comparable in magnitude to their amplitudes. In the onshore region, this normalized variance saturates at a number less than one, indicating that the common wind forcing results in similar solutions over the shelf, despite the imposed differences in boundary conditions. The saturation value for this norm in the onshore region is roughly 0.5–0.7, somewhat larger than for the wind-analysis ensemble.

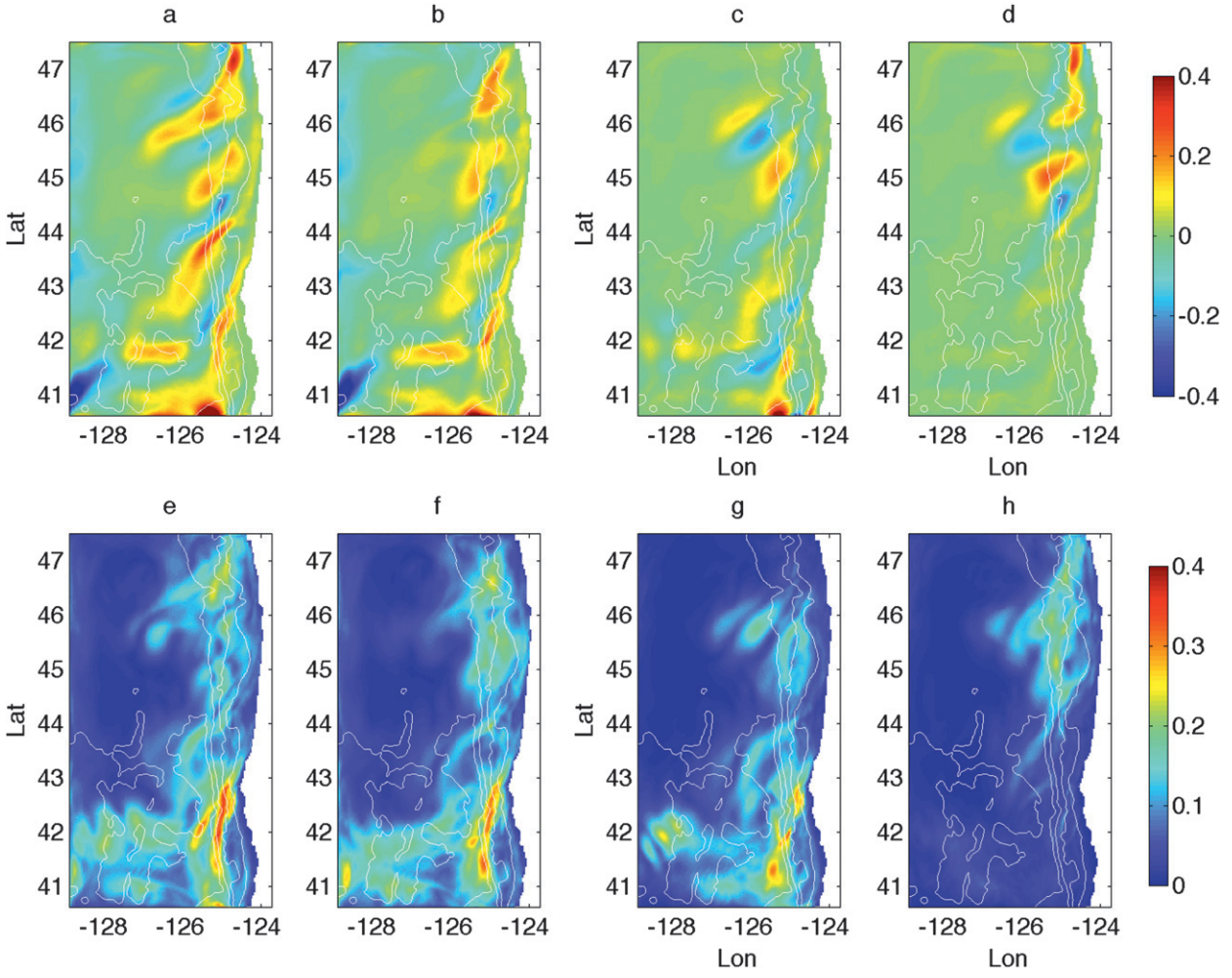

FIG. 11. (top) Time and ensemble mean and (bottom) standard deviation of velocity vector differences with $A(t)$ vs longitude and latitude for (a),(e) $\mathbf{B}_1$; (b),(f) $\mathbf{B}_2$; (c),(g) $\mathbf{B}_3$; and (d),(h) $\mathbf{B}_4$ relative to the unperturbed simulation. In each case, the ensemble average is computed over the three simulations with different realizations of ψ_n.

For these 110-day simulations, evidence for propagation of boundary disturbances along the shelf is apparent in the time- and ensemble-averaged mean and standard deviations of the differences of boundary-perturbed fields from the basic-case simulation, for variables such as surface velocity (Fig. 11). For all boundary perturbations, most of the mean difference is concentrated along the shelf and slope, except south of Cape Blanco (43°N), where the disturbances extend far offshore, reaching to the western boundary of the computational domain. For the southern ($\mathbf{B}_3$) and northern ($\mathbf{B}_4$) perturbations, the mean differences are concentrated in the southern and northern parts of the domain, respectively, while for the western ($\mathbf{B}_2$) perturbation, the amplitude of the response over the shelf and slope is somewhat reduced from that for the full ($\mathbf{B}_1$) perturbation but is otherwise similar to it. This suggests that offshore boundary differences from the western ($\mathbf{B}_2$) perturbation may propagate along the computational open boundary to the shelf. The time- and ensemble-averaged standard deviations of the difference fields show similar behavior to the mean differences, but with notably more offshore extension of the difference fields for all boundary perturbation cases (bottom panels in Fig. 11). The more limited southward penetration of the northern ($\mathbf{B}_4$) perturbations, relative to the southern ($\mathbf{B}_3$) perturbations, presumably reflects the relative inefficiency of advection associated with the southward coastal jet, compared to northward-propagating coastal-trapped wave processes, in transporting boundary perturbations along the shelf.

The short-term response along the 75-m isobath is direct evidence for this propagation (Fig. 12). Over the first 20 days of the perturbation simulations (days 180–200), the perturbation at the northern boundary is

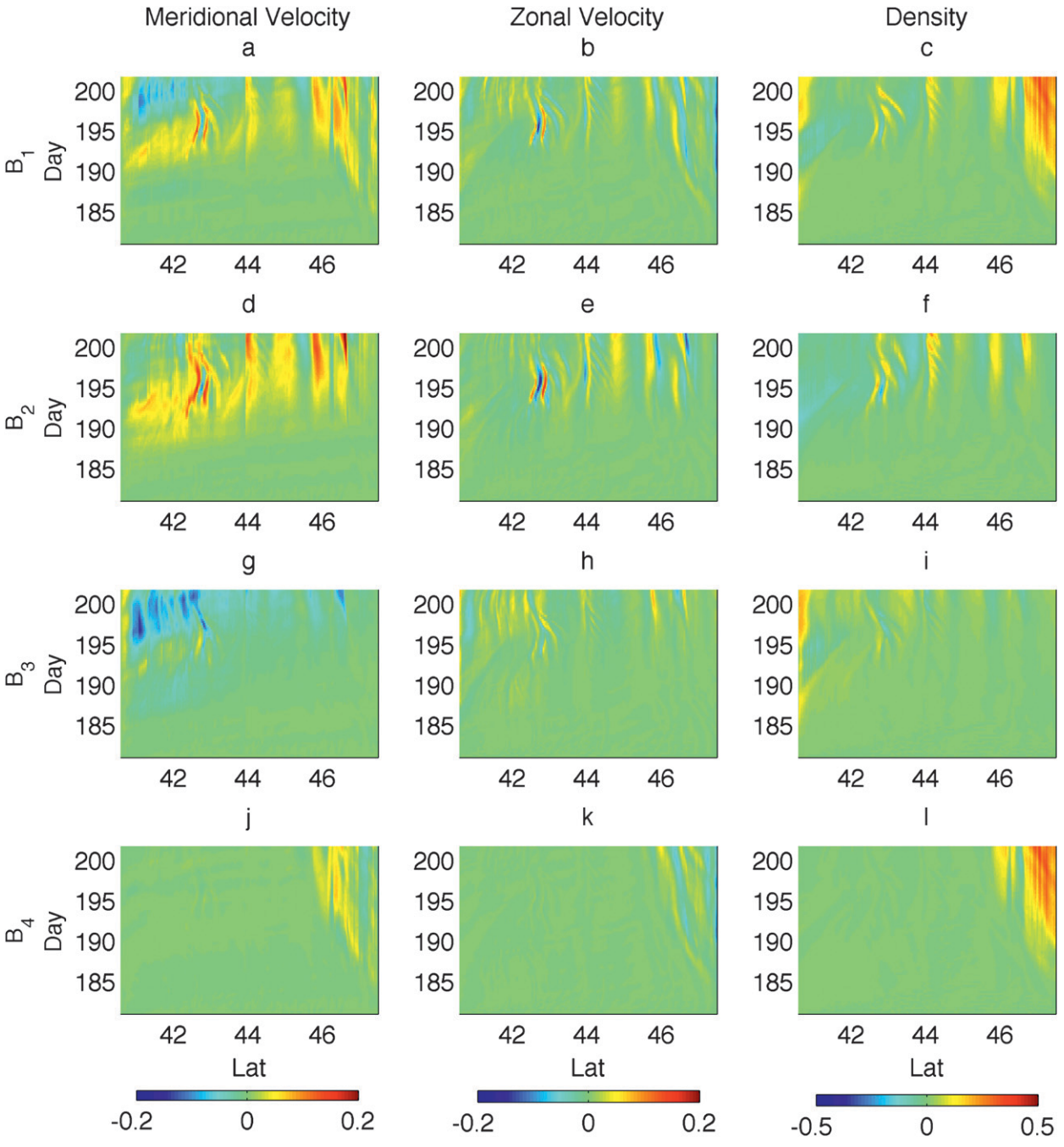

FIG. 12. Ensemble-averaged (left) meridional velocity, (middle) zonal velocity, and (right) density differences along the 75-m isobath vs latitude and time for perturbed boundary condition simulations (a),(b),(c) $\mathbf{B}_1$; (d),(e),(f) $\mathbf{B}_2$; (g),(h),(i) $\mathbf{B}_3$; and (j),(k),(l) $\mathbf{B}_4$ relative to the unperturbed simulation. In each case, the ensemble average is computed over the three simulations with different realizations of ψ_n.

advected southward at a mean speed of roughly 10–20 cm s^{-1}, reaching 45°N at day 200. The perturbation at the southern boundary appears to extend somewhat farther into the domain and to propagate somewhat more rapidly, reaching 43°N by day 193 or earlier. While this stronger and faster influence of southern, relative to northern, boundary perturbations is broadly consistent with expectations from coastal-trapped wave dynamics, low-mode coastal-trapped waves apparently do not dominate the signal. Such waves would propagate

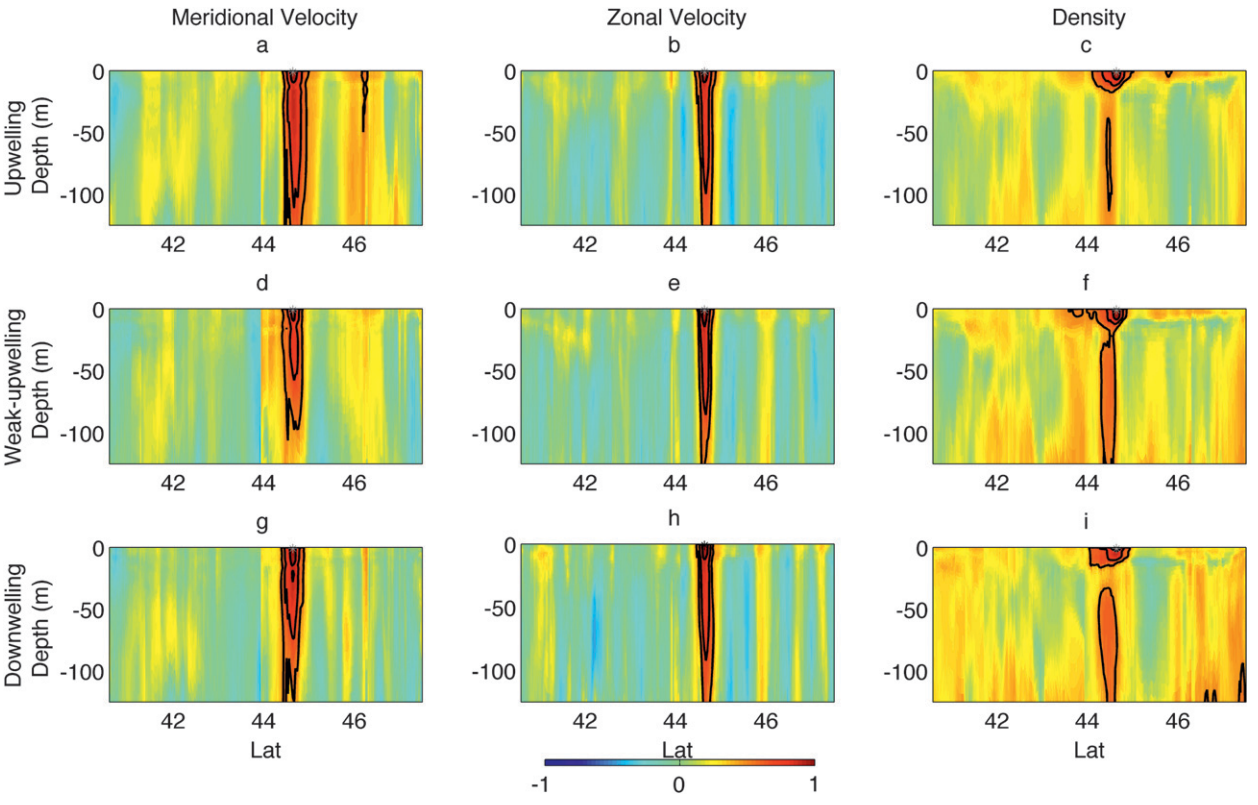

FIG. 13. Correlations of (left) meridional velocity, (middle) zonal velocity, and (right) density at each point along the 200-m isobath with the same variable at the surface (asterisk) vs depth and longitude along the Newport line (44.65°N) during (a)–(c) upwelling, (d)–(f) weak-upwelling, and (g)–(i) downwelling periods. The 0.5, 0.7, and 0.9 contours are shown (black lines).

at roughly 3 m s^{-1}, or 300 km day^{-1}, and reach the northern boundary in roughly 2 days. On the other hand, mean advection along the 75-m isobath is southward (Fig. 3b), so the northward intrusion of disturbances from the southern boundary must evidently involve a combination of northward wave propagation and southward advection.

It is difficult to separate the disturbance variance in the different cases into components that are directly forced by the boundary perturbations, and components that arise from internal instabilities developing from the forced perturbations. On the other hand, the existence of differences in total disturbance variance in the various cases, and the systematically larger ensemble spread for the case $\mathbf{B}_1$ of full boundary forcing, suggests that the directly forced component is significant. To the extent that this is true, it may be appropriate to compute the relative importance of boundary perturbations by normalizing the interior variance by the total boundary perturbation variance for each case $\mathbf{B}_1$, $\mathbf{B}_2$, $\mathbf{B}_3$, and $\mathbf{B}_4$. From this perspective, the shelf-slope perturbations $\mathbf{B}_3$ and $\mathbf{B}_4$ are much more efficient sources of interior error variance than are the full or western perturbations $\mathbf{B}_1$ and $\mathbf{B}_2$.

6. Covariances

The main focus of this study, described in the preceding sections, has been the analysis of coastal ocean model uncertainty and its relation to sources of error from surface forcing, initial, and boundary conditions. A related aspect of the model error fields that is of interest is their spatial correlation structure, the covariability of errors at one point with those at another point. These correlations are fundamental to most data assimilation schemes, and can be directly computed from ensembles of simulations. For example, Oke et al. (2002b) computed such correlations for ensembles obtained from simulations forced by a set of observed wind records from different summers; the result was an estimate of the covariation of errors that is intrinsic to the ocean dynamics, when the forcing fields are completely independent.

In this section, we use the wind-analysis ensemble described above to compute the cross correlations associated with the ocean-state errors that develop in response to small, but systematic, errors in the winds; as described above, the amplitude and structure of the effective wind error was estimated from operational analysis differences.

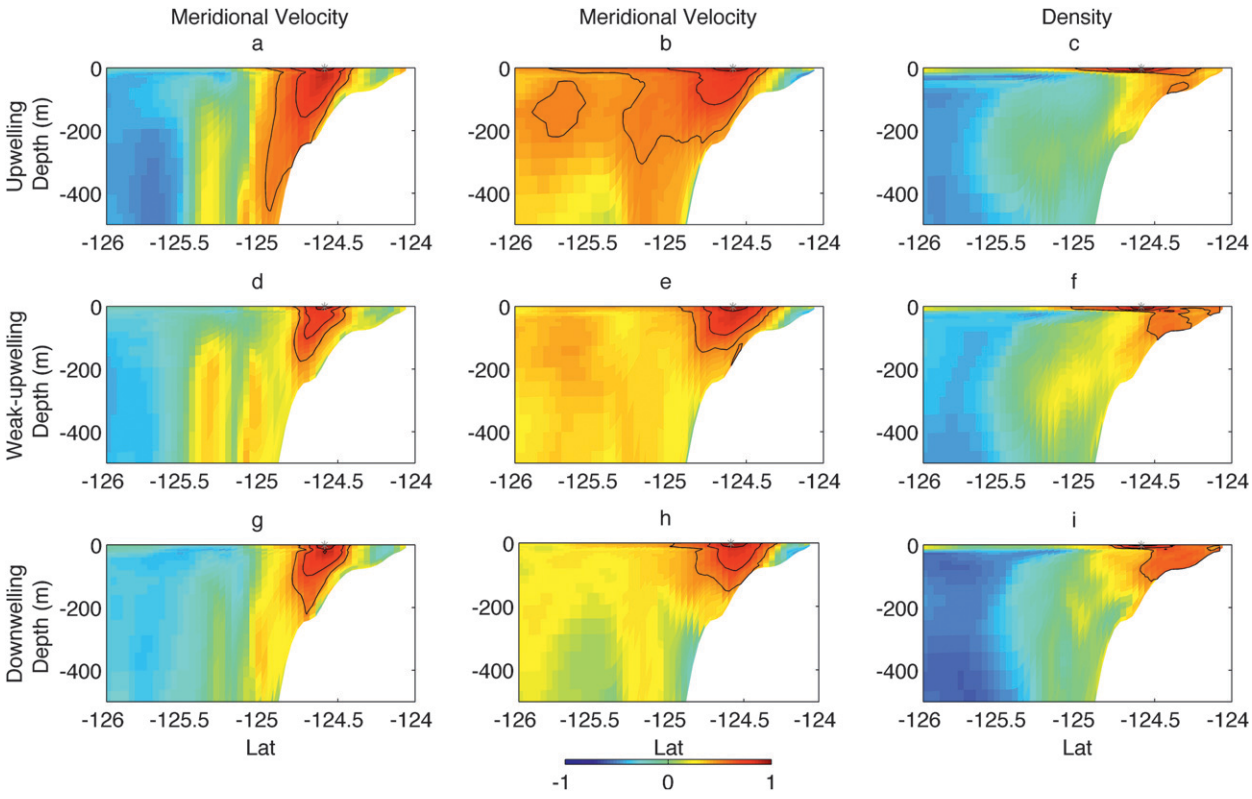

FIG. 14. Correlations of (left) meridional velocity, (middle) zonal velocity, and (right) density at each point vs depth and longitude along the Newport line (44.65°N) with the same variable at the surface (asterisk) at the 200-m isobath during (a)–(c) upwelling, (d)–(f) weak-upwelling, and (g)–(i) downwelling periods. The 0.5, 0.7, and 0.9 contours are shown (black lines).

This procedure should provide a better representation of actual error statistics than estimates based on the full variation of the ocean fields, with fully independent forcing fields, such as those of Oke et al. (2002b). If, in a data-assimilating hindcast simulation of the coastal ocean circulation forced by analyzed winds, the dominant error in the ocean state were the result of errors in the wind fields, and if the present ensemble-based estimate of the wind-analysis errors were approximately accurate, then it would be appropriate to use these correlation fields in the assimilation. In the process, we use the wind-analysis ensemble to explore a possible state dependence of the covariance structure.

The correlation fields were obtained from the wind-analysis ensemble, described above in section 3, as follows. First, the differences of each member of the ensemble of ocean simulations from the ensemble mean at each time were computed. To address the possible state dependence of the correlations, the difference time series were then segregated into periods of upwelling, weak-upwelling, and downwelling winds. These periods were defined in terms of the domain-averaged meridional wind: upwelling when this averaged wind was southward at greater than 5 m s^{-1}, weak-upwelling it was southward between 4 and 1 m s^{-1}, and downwelling when it was northward and greater than 1 m s^{-1}. These three categories corresponded to 47%, 21%, and 14%, respectively, of the simulation time period. For each given time in each of these periods, correlations between variables at different points and among different ensemble members were computed from the differences, with normalization by the respective standard deviations. Finally, the correlation fields were time averaged for each period.

The correlation fields over the shelf (Figs. 13, 14, and 15), the region of primary interest here, show two main results: in general, the estimated correlation scales appear to be broadly similar to those obtained by Oke et al. (2002b), despite the substantial differences in procedure, and the correlation structure appears to have no strong state dependence. Alongshore (Fig. 13) and cross-shore (Fig. 14) autocorrelation scales for horizontal velocity and density are of order several tens of kilometers, while the vertical scale is of the order of the local fluid depth. There is a hint of much longer correlation alongshore correlation scales for density, perhaps generally consistent with some of the cross-correlation structure presented by Oke et al. (2002b; their Fig. 7). The strongest state dependence in the autocorrelations is in the cross-shore

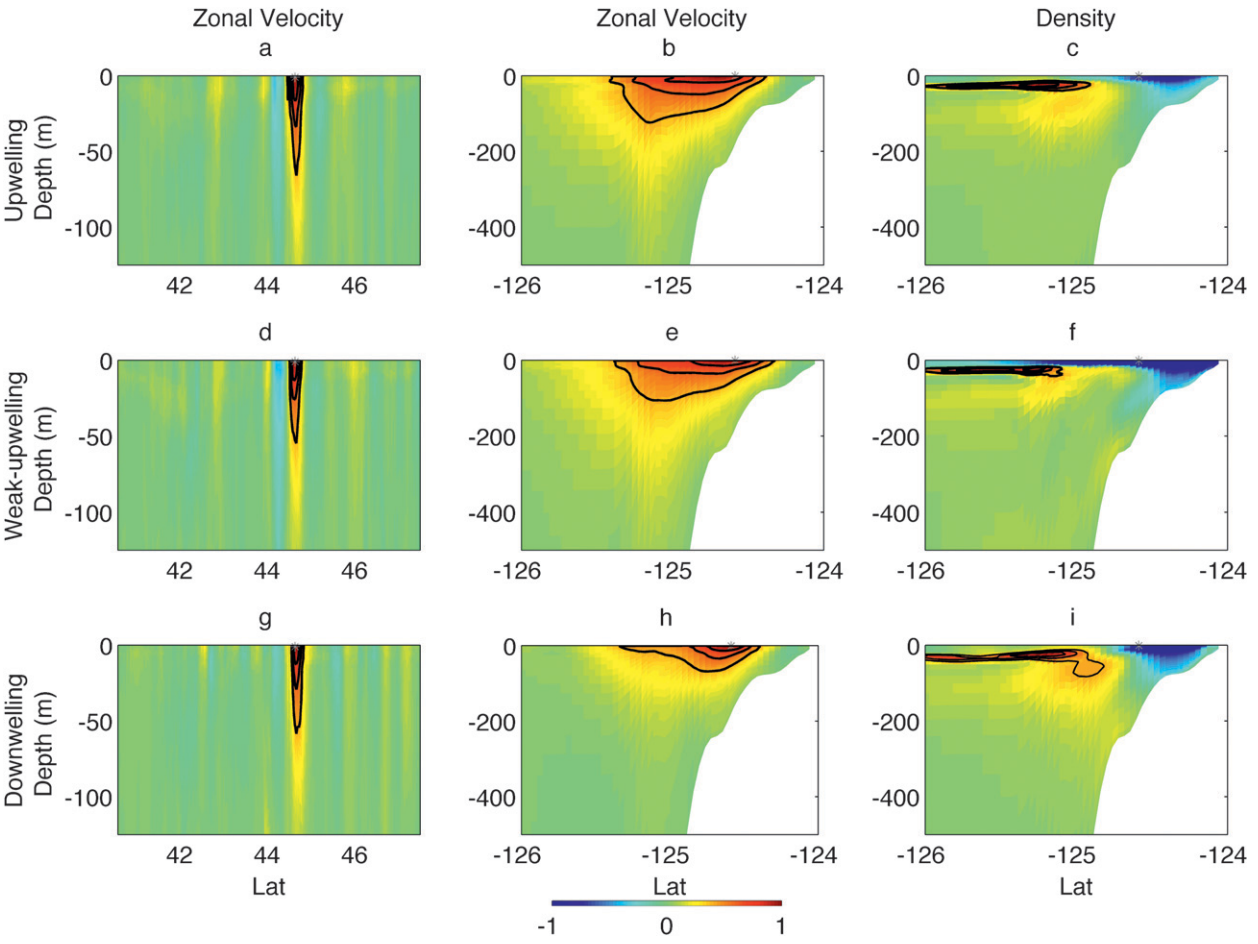

FIG. 15. Cross-correlations of (left),(middle) zonal velocity and (right) density at the surface (asterisk) on the 200-m isobath at the Newport line (44.65°N) with meridional velocity vs depth and (left) latitude along the 200-m isobath and (middle),(right) longitude along the Newport line during (a)–(c) upwelling, (d)–(f) weak-upwelling, and (g)–(i) downwelling periods. The 0.4, 0.6, and 0.8 contours are shown (black lines).

structure of the horizontal velocity autocorrelation, for which the scales during the upwelling periods are up to twice as large as those for the weak-upwelling and downwelling periods (Fig. 14).

The cross-correlation fields have smaller correlation scales than the autocorrelation fields; for example, correlations of meridional velocity with zonal velocity and density have vertical scales of only a few tens of meters, substantially less than the local fluid depth (Fig. 15). The cross-shore cross sections of the cross correlations of meridional velocity with density show an offshore sign reversal that is generally consistent with geostrophic balance (Figs. 15c,f and i). In general, state dependence of the cross-correlation fields is also weak, with perhaps some indication of differences in vertical correlation scales for the cross correlations between meridional velocity and zonal velocity or density (Fig. 15).

7. Summary

In the present paper, a series of ensemble simulations have been performed with well-known wind forcing in order to understand the impact on ocean states in the coastal ocean model of the uncertainties on different components: poorly known or known initial conditions, and open-boundary conditions perturbed at different location. The analysis of the resulting simulation ensembles represents a modest step toward the development of an uncertainty budget for a coastal ocean model in a wind-forced regime. While other processes may dominate the budget in other coastal flow regimes, we hope that the approach taken here will contribute to the development of a useful, general framework for the analysis of uncertainty in coastal circulation models.

Given well-predicted wind forcing with a realistic estimated error, the accuracy of the ocean state prediction

was seen to depend on the geographical regions, with shelf and slope-interior regimes distinguished by the nominal 200-m isobath. In the shelf region, the circulation shows a more deterministic response to the wind forcing than over the slope, such that the uncertainty saturates at a normalized value near 0.4, for wind-forcing errors estimated from analysis differences.

Consideration of the adjustment from poorly known initial conditions indicates that the time scale of approach toward the saturated state over the shelf is roughly 1 week. In the slope-interior regime, errors that are small initially grow slowly, but persistently, until no information from the initial conditions remains after a period of order 2–3 months. There is evidence from the simulation ensembles for interaction of the shelf and slope-interior regimes, with ensemble variance in the shelf regime being partially maintained through the influence of slope-interior variability.

Over the 6-month time span of these simulations, the penetration of boundary condition errors into the domain was seen to occur primarily along the shelf and slope. The extent of this penetration depended on the location of the boundary perturbations, with the smallest absolute effect observed in response to perturbations confined to the shelf region along the northern boundary. Normalized by the total variance along the boundary, however, the perturbations confined to the shelf region along the southern and northern boundaries, respectively, had the strongest effects on the interior circulation.

These results have a variety of implications for interpretation, modeling, and practical prediction of coastal ocean circulation. The results from the wind-analysis ensemble indicate that numerical prediction of coastal ocean circulation over wind-driven shelves with significant, though also limited, skill should be achievable with models that are forced with operational wind fields and are initialized only with previous forecast fields and with no assimilation of ocean data. This deterministic element of the shelf response over the Oregon coast where strong wind-driven flows are prevailing is generally consistent with the well-known success of linear, forced-damped, coastal-trapped wave models in hindcasting large fractions of observed coastal sea level and alongshore velocity variance under similar conditions. The different behavior of the slope-interior regime suggests that successful prediction of offshore circulation features will depend heavily on accurate initialization, and thus on the availability of data and the implementation of optimal data assimilation methods. The dependence on boundary perturbations suggests that, for regional coastal ocean modeling, special attention must be paid to the specification of accurate boundary information along the open boundaries over the shelf and slope, at both the poleward and equatorward edges of the regional domain. The indications of interaction between the shelf and slope regimes point toward the need for new understanding of the associated dynamical processes, which remain poorly understood and relate directly to the important general problem of shelf-interior exchange of fluid physical properties and dissolved and suspended biological and chemical matter.

Acknowledgments. This research was supported by the Office of Naval Research (Grant N00014-05-1-0891) through the National Ocean Partnership Program. The wind products of year 2008 were obtained from the THORPEX Interactive Grand Global Ensemble (TIGGE) data archive.

REFERENCES

Barth, A., A. Alvera-Azcàrate, and R. H. Weisberg, 2008: Assimilation of high-frequency radar currents in a nested model of the West Florida Shelf. *J. Geophys. Res.,* **113,** C08033, doi:10.1029/2007JC004585.

Barth, J. A., S. D. Pierce, and R. L. Smith, 2000: A separating coastal upwelling jet at Cape Blanco, Oregon, and its connection to the California Current System. *Deep-Sea Res.,* **47,** 783–810, doi:10.1016/S0967-0645(99)00127-7.

Bèal, D., P. Brasseur, J. M. Brankart, Y. Ourmières, and J. Verron, 2010: Characterization of mixing errors in a coupled physical biogeochemical model of the North Atlantic: Implications for nonlinear estimation using Gaussian anamorphosis. *Ocean Sci.,* **6,** 247–262.

Beckmann, A., and D. B. Haidvogel, 1993: Numerical simulation of flow around a tall isolated seamount. Part I: Problem formulation and model accuracy. *J. Phys. Oceanogr.,* **23,** 1736–1753.

Broquet, G., P. Brasseur, D. Rozier, J. M. Brankart, and J. Verron, 2008: Estimation of model errors generated by atmospheric forcings for ocean data assimilation: Experiments in a regional model of the Bay of Biscay. *Ocean Dyn.,* **58,** 1–17.

Burillo, I. A., G. Caniaux, M. Gavart, P. De Mey, and R. Baraille, 2002: Assessing ocean-model sensitivity to wind forcing uncertainties. *Geophys. Res. Lett.,* **29,** 1858, doi:10.1029/2001GL014473.

Castelao, R. M., and J. A. Barth, 2005: Coastal ocean response to summer upwelling favorable winds in a region of alongshore bottom topography variations off Oregon. *J. Geophys. Res.,* **110,** C10S04, doi:10.1029/2004JC002409.

Chapman, D. C., 1985: Numerical treatment of cross-shelf open boundaries in a barotropic coastal ocean model. *J. Phys. Oceanogr.,* **15,** 1060–1075.

Ehrendorfer, M., and R. M. Errico, 1995: Mesoscale predictability and the spectrum of optimal perturbations. *J. Atmos. Sci.,* **52,** 3475–3500.

Fairall, C. W., E. F. Bradley, D. P. Rogers, J. B. Edson, and G. S. Young, 1996: Bulk parameterization of air-sea fluxes for tropical ocean-global atmosphere coupled-ocean atmosphere response experiment. *J. Geophys. Res.,* **101,** 3747–3764.

Flather, R. A., 1976: A tidal model of the northwest European continental shelf. *Mern. Soc. Roy. Sci. Liege Ser.,* **6** (10), 141–164.

Jordà, G., and P. De Mey, 2010: Characterization of error dynamics in a 3D coastal model of the Catalan sea using stochastic modelling. *Cont. Shelf Res.,* **30** (5), 419–441.

Kim, S., R. M. Smelson, and C. Snyder, 2009: Ensemble-based estimates of the predictability of wind-driven coastal ocean flow over topography. *Mon. Wea. Rev.,* **137,** 2515–2537.

Kindle, J. C., R. M. Hodur, S. deRada, J. D. Paduan, L. K. Rosenfeld, and F. Q. Chavez, 2002: A COAMPS™ reanalysis for the Eastern Pacific: Properties of the diurnal sea breeze along the central California coast. *Geophys. Res. Lett.,* **29,** 2203, doi:10.1029/2002GL015566.

Kosro, P. M., 2005: On the spatial structure of coastal circulation off Newport, Oregon, during spring and summer 2001 in a region of varying shelf width. *J. Geophys. Res.,* **110,** C10S06, doi:10.1029/2004JC002769.

Kurapov, A. L., J. S. Allen, G. D. Egbert, and R. N. Miller, 2005a: Modeling bottom mixed layer variability on the mid-Oregon Shelf during summer upwelling. *J. Phys. Oceanogr.,* **35,** 1629–1649.

——, ——, ——, ——, P. R. Kosro, M. D. Levine, and T. J. Boyd, 2005b: Distant effect of assimilation of moored currents into a model of coastal wind- driven circulation of Oregon. *J. Geophys. Res.,* **110,** C02022, doi:10.1029/2003JC002195.

Leeuwenburgh, O., 2005: Assimilation of along-track altimeter data in the tropical Pacific region of a global OGCM ensemble. *Quart. J. Roy. Meteor. Soc.,* **131,** 2455–2472.

Loève, M., 1978: Probability theory. *Graduate Texts in Mathematics,* 4th ed. J. H. Ewing, F. W. Gehring, and P. R. Halmos, Eds., Vol. 46, Springer-Verlag, 3–391.

Lucas, M. A., N. Ayoub, B. Barnier, T. Penduff, and P. de Mey, 2008: Stochastic study of the temperature response of the upper ocean to uncertainties in the atmospheric forcing in an Atlantic OGCM. *Ocean Modell.,* **20,** 90–113.

Mellor, G. L., and T. Yamada, 1982: Development of a turbulence closure model for geophysical fluid problems. *Rev. Geophys. Space Phys.,* **20,** 851–875.

Mourre, B., P. De Mey, F. Lyard, and C. Le Provost, 2004: Assimilation of sea level data over continental shelves: an ensemble method for the exploration of model errors due to uncertainties in bathymetry. *Dyn. Atmos. Oceans,* **38,** 93–121.

National Geophysical Data Center, 1988: Data Announcement 88-MGG-02, Digital relief of the Surface of the Earth. NOAA, NGDC, Boulder, CO. [Available online http://www.ngdc.noaa.gov/mgg/global/etopo5.HTML.]

Oke, P. R., J. S. Allen, R. N. Miller, and G. D. Egbert, 2002a: A modeling study of the three-dimensional continental shelf circulation off Oregon. Part II: Dynamical balances. *J. Phys. Oceanogr.,* **32,** 1383–1403.

——, ——, ——, ——, and P. R. Kosro, 2002b: Assimilation of surface velocity data in to a primitive equation coastal ocean model. *J. Geophys. Res.,* **107,** 3122, doi:10.1029/2000JC000511.

——, and Coauthors, 2002c: A modeling study of the three-dimensional continental shelf circulation off Oregon. Part I: Model-data comparisons. *J. Phys. Oceanogr.,* **32,** 1360–1382.

Perlin, N., R. M. Samelson, and D. B. Chelton, 2004: Scatterometer and model wind and wind stress in the Oregon–northern California coastal zone. *Mon. Wea. Rev.,* **132,** 2110–2129.

Samelson, R. M., and Coauthors, 2002: Wind stress forcing of the Oregon coastal ocean during the 1999 upwelling season. *J. Geophs. Res.,* **107,** 3034, doi:10.1029/2001JC000900.

Shchepetkin, A. F., and J. C. McWilliams, 2005: The Regional Ocean Modeling System: A split-explicit, free-surface, topography-following coordinate ocean model. *Ocean Modell.,* **9,** 347–404.

Shulman, I., J. C. Kindle, S. deRada, S. C. Anderson, B. Penta, and P. J. Martin, 2004: Development of a hierarchy of nested models to study the California current system. *Estuarine and Coastal Modeling 2003: Eighth International Conference on Estuarine and Coastal Modeling,* M. L. Spaulding, Ed., American Society of Civil Engineering, 74–88.

Song, Y., and D. B. Haidvogel, 1994: A semi-implicit ocean circulation model using a generalized topography-following coordinate system. *J. Comput. Phys.,* **115,** 228–244.

Springer, S. R., R. M. Samelson, J. S. Allen, G. D. Egbert, A. L. Kurapov, R. N. Miller, and J. C. Kindle, 2009: A nested grid model of the Oregon coastal transition zone: Simulations and comparisons with observations during the 2001 upwelling season. *J. Geophys. Res.,* **114,** C02010, doi:10.1029/2008JC004863.

Sutton, C., T. M. Hamill, and T. T. Warner, 2006: Will perturbing soil moisture improve warm-season ensemble forecasts? A proof of concept. *Mon. Wea. Rev.,* **134,** 3174–3189.

Vandenbulcke, L., M. Rixen, J.-M. Beckers, A. Alvera-Azcàrate, and A. Barth, 2008: An analysis of the error space of a high-resolution implementation of the GHER hydrodynamic model in the Mediterranean Sea. *Ocean Modell.,* **24,** 46–64.

Vukićević, T., and R. M. Errico, 1990: The influence of artificial and physical factors upon predictability estimates using a complex limited-area model. *Mon. Wea. Rev.,* **118,** 1460–1482.

Zhang, F., C. Snyder, and R. Rotunno, 2003: The influence of moist convection on the limits of mesoscale predictability. *J. Atmos. Sci.,* **60,** 1173–1185.